Effect of Passivating Shells on the Chemistry and Electrode Properties of LiMn2O4 Nanocrystal Heterostructures

Journal:	*ACS Applied Materials & Interfaces*
Manuscript ID	am-2018-146689.R1
Manuscript Type:	Article
Date Submitted by the Author:	06-Nov-2018
Complete List of Authors:	Kwon, Bob Jin; University of Illinois at Chicago Dogan, Fulya; Argonne National Laboratory, Chemical Science and Engineering Division Jokisaari, Jacob; University of Illinois at Chicago, Department of Physics Key, Baris; Argonne National Laboratory, Chemical Sciences and Engineering Division Kim, Chunjoong; Chungnam National University, Materials science and Engineering Liu, Yi-Sheng; E O Lawrence Berkeley National Laboratory, Guo, Jinghua; E O Lawrence Berkeley National Laboratory, Advanced Light Source Klie, Robert; University of Illinois at Chicago, Department of Physics Cabana, Jordi; University of Illinois at Chicago, Department of Chemistry

Effect of Passivating Shells on the Chemistry and Electrode Properties of $LiMn_2O_4$ Nanocrystal Heterostructures

Bob Jin Kwon,[a] Fulya Dogan,[b] Jacob R. Jokisaari,[c] Baris Key,[b] Chunjoong Kim,[d] Yi-Sheng Liu,[e] Jinghua Guo,[e,f] Robert F. Klie[c] and Jordi Cabana[*a]

[a]Department of Chemistry, University of Illinois at Chicago, Chicago, IL 60607, United states

[b]Chemical Science and Engineering Division, Argonne National Laboratory, Argonne, IL 60439, United states

[c]Department of Physics, University of Illinois at Chicago, Chicago, IL 60607, United states

[d]School of Material Science and Engineering, Chungnam National University, Daejeon, 305-764, Republic of Korea

[e]Advanced Light Source, Lawrence Berkeley National Laboratory, Berkeley, CA 94720, United states

[f]Department of Chemistry and Biochemistry, University of California, Santa Cruz, CA 95064, United states

KEYWORDS

Cathode/electrolyte interface, Al-rich passivating layers, heterostructure nanocrystals, spinel $LiMn_2O_4$, Li-ion batteries

ABSTRACT

Building a stable chemical-environment at the cathode/electrolyte interface is directly linked to the durability of Li-ion batteries with high energy density. Recently, colloidal chemistry methods have enabled the design of core-shell nanocrystals of $Li_{1+x}Mn_{2-x}O_4$, an important battery cathode, with passivating shells rich in Al^{3+} through a colloidal synthetic route. These heterostructures combine the presence of redox inactive ions on the surface to minimize undesired reactions, with the coverage of each individual particle in an epitaxial manner. While they improve electrode performance, the exact chemistry and structure of the shell, as well as the precise effect of the ratio between the shell and the active core remain to be elucidated. Correlation of these parameters to electrode properties would serve to tailor the heterostructure design toward complete shutdown of undesired reactions. These knowledge gaps are the target of this study. $Li_{1+x}Mn_{2-x}O_4$ nanocrystals with Al^{3+}-rich shells of different thickness were synthesized. Multi-modal characterization comprehensively revealed the elemental distribution, electronic state and crystallinity in the heterostructures, which confirmed the potential of this approach to finely tune passivating layers. All the modified nanocrystals improved the capacity retention while retaining charge storage compared to the bare counterpart, even under harsh conditions.

1. INTRODUCTION

Lithium-ion batteries are considered as the most efficient energy storage system to power electrical drive vehicles, due to their high power and energy density.[1,2] Among the many energy storage materials, spinel-type $Li_{1+x}Mn_{2-x}O_4$ is a mature choice for the cathode due to its high operating potential (> 4.0 V vs Li^+/Li^0), robust durability and power capability.[3,4] However, this oxide suffers from interfacial instabilities, mainly derived from dissolution of Mn from the surface, through a disproportionation reaction triggered by the presence of acidic impurities present in the electrolyte, and generated during cycling.[5,6] These undesired interfacial processes induce fading of the storage capacity, especially at above standard temperature, which occurs in real life applications. Therefore, the development of a material suitable for more widespread applications in electric vehicles requires identifying avenues to suppress interfacial reactions to further enhance durability, while preserving high energy storage and power capability. Replacing transition metal ions with redox-inactive ions can create stable interfaces by reducing the unwanted side reactions associated with corrosion/dissolution and the redox activity of the surfaces.[7] However, this substitution must take place in the form of very thin layers to avoid an unacceptable loss of capacity for charge storage and electronic conductivity. Furthermore, these layers must completely cover each single particle to avoid exposure of buried and unprotected surfaces during inevitable particle shuffling upon battery cycling.[8] Lastly, the specific structure of these layers needs to be controlled to minimize barriers to ionic conduction, which would create kinetic impediments to the transfer of Li ions to/from the electrolyte. All in all, careful tailoring the chemical composition, conformality and thickness of the layers of surface modification on particles of a battery cathode is pivotal to improving its electrochemical properties. This goal challenges our current ability to synthesize and assemble complex multifunctional structures at the level of single particles.

Various methods and materials have been applied in an attempt to achieve the ideal surface modifications. Chemical vapor deposition (CVD), atomic laser deposition (ALD), and methods based on wet chemistry, such as sol gel, are arguably the most common.[9-11] However, while they theoretically lead to conformal layers and robust control of chemistry, these post-synthetic methods are typically employed to modify aggregated powders, which present extremely uneven surface roughness and a significant density of buried interfaces connected, at best, by highly tortuous porosity. The use of these powders as substrates for deposition of protective layers creates inherent limitations on the ability to passivate all potential interfaces and the homogeneity of any applied layers, especially given the possible inter-diffusion of elements during subsequent annealing to remove residual precursors.[12] The lack of control of the physical and chemical features of the shells due to the inadequacy of the substrates creates inefficient formation of protective layers, and reduces the energy density through the excessive use of inactive chemical species. Recently, our group designed a strategy to prepare nanocrystal heterostructures containing a ~18 nm core of spinel $Li_{1+x}Mn_{2-x}O_4$ covered by a ~2 nm shell where Al were replaced by Mn while preserving structural epitaxy.[13] To establish an optimum core-shell architecture, a colloidal synthetic route was designed to grow the thin shell enriched with Al^{3+} on the individual nanocrystals while they were present in fully dispersible form in a solution containing a surfactant, thus ensuring conformal coverage of all nanocrystals. The core-shell nanocrystals showed improved cycling stability even at high temperature and resistance to corrosion by acidic environments, while maintaining similar levels of storage capacity as bare counterparts. However, only one core-shell ratio was attempted. Together with an insufficient understanding of the exact chemical states of Mn and Al, and their distribution in the heterostructures, correlations with electrochemical performance that underpin rules of design could not be established. As an example, it would be desirable to increase the volume of the core while maintaining shell thickness in order to further reduce the total amount of inactive Al in the oxide. Broadly, the careful control and morphological homogeneity of colloidal chemistry turns the resulting heterostructures into useful model systems to study the fundamental effect of surface modifications on stabilities and electrode kinetics.

In this report, the colloidal synthetic method was redesigned to grow passivating layers containing Al^{3+} at varying thicknesses, on nanocrystal cores that were ~60 nm. Control of the bulk structure and composition was achieved to make comparisons of electrode stability where only the characteristics of the shell were a variable.[14,15] Each individual spinel nanocrystal then presents an ultra-thin shell, consisting of a gradient of concentration of Al on the surface, revealed by electron microscopy. Through a combination of spectroscopy and microscopy, this study further reveals the effect of the shells on the local structure of the spinel domains, as well as the variety of chemical states in which Mn and Al are found in the heterostructure. In all cases, the modified crystals show enhanced capacity retention with respect to the contents of passivating shells. The effect of shell thickness and composition on storage capacity and rate capability was established, providing valuable insight, broadly, into design rules for protective layers on battery cathodes.

2. EXPERIMENTAL SECTION

2.1. Synthetic procedure

The procedure to prepare core-shell nanocrystals is summarized in Scheme S1. Precursor MnO nanocrystals were prepared by a colloidal synthetic method. First, 4 mM Mn (II) acetate

(Product No. 330825, Sigma-Aldrich) was dissolved in a 30 mL of oleylamine (OAm) solution (Product No. O7805, Sigma-Aldrich) at room temperature under a nitrogen blanket in a Schlenk line. The mixture was subsequently degassed at 100 ℃ for 20 minutes under vacuum, followed by heating at 250 ℃ for 3 hours in nitrogen, under strong magnetic stirring. In order to introduce the Al-based shells, when the vessel was first cooled to 220 ℃, 20 ml of OAm solution containing aluminum acetylacetonate (Product No. 208248, Sigma-Aldrich) were added dropwise into the colloidal solution. The concentration of aluminum acetylacetonate was selected as 0.2, 0.4 and 0.8 mM (0.0648, 0.1297, and 0.2594 g) to evaluate the effect of the Al content in the protective layers. The corresponding core-shell manganese oxide precursors are labelled as CS-MnO 1, 2, and 3, respectively. The solution was further annealed for 2 hours at 220 ℃ to form an aluminum oxide layer overcoating all the nanocrystals. Finally, the resulting nanocrystals were cooled to room temperature, collected by centrifugation for 5 minutes at 10000 rpm, re-dispersed in 15 ml of hexane and washed with 20 ml of ethanol, followed by centrifugation. This process was repeated four times. After washing the nanocrystals, the powder was dried overnight at 60 ℃. In order to prepare Li-containing oxides, the nanocrystals were thoroughly mixed with lithium acetate (Product No. 517992, Sigma-Aldrich) at different ratios of Li and Mn, and calcined in air at 600 ℃ for 4 hours, with a ramping rate of 5 ℃/min. Throughout this report, bare LMO and CS-LMO are used as labels for the products without and with Al shells, respectively. CS-LMO 1, 2 and 3 represent the modified spinel samples prepared from the CS-MnO 1, 2 and 3 precursors, respectively.. Detailed synthetic conditions can be found in Table S1.

2.2. Characterization

Powder X-ray diffraction was performed on a Bruker D8 Avance using Cu Kα (λ_{avg}=1.5418 Å) radiation. Scan rates were 0.04 ° s^{-1} from 10° to 80 ° (2θ). Fitting of the patterns to calculate lattice parameters of the different samples was carried out using GSAS-II.

Scanning electron microscopy was conducted on a Hitachi S-3000N, fitted with energy dispersive X-ray (EDX) detector. Transmission electron microscopy at low magnification was carried out on a JEOL JEM 3010, operated at 300 kV. The images were analysed to extract the distribution of particle size by measuring approximately 200 nanocrystals using ImageJ from the Research Services Branch of NIMH & NINDS. All scanning transmission electron microscopy STEM) imaging and energy dispersive X-ray (EDX) spectroscopy were performed on an aberration-corrected JEOL JEM-ARM200CF, operated at 200 kV, which can achieve a spatial resolution of ~73 pm. Images were acquired in high-angle annular dark field (HAADF), low angle annular dark field (LAADF) and annular bright field (ABF) mode. In HAADF imaging, the resulting contrast is approximately Z^2. The ARM200CF is equipped with an Oxford X-Max 100TLE windowless silicon drift EDX detector. Electron energy-loss spectroscopy (EELS) was performed at the Mn $L_{II,\,III}$-edges at an acceleration voltage of 200 kV. The background was removed and normalized using Digital Micrograph™ software by Gatan Inc.

Mn *L*- and O *K*-edge X-ray absorption spectroscopy (XAS) measurements were carried out at beamline 6.3.1.2 ISAAC endstation at the Advanced Light Source (ALS) at Lawrence Berkeley National Laboratory. Spectra were collected in total electron yield (TEY) and total fluorescence yield (TFY) modes at room temperature and under ultra-high vacuum conditions (below 10^{-8} Torr). Contributions from visible light were carefully minimized before the acquisition, and all spectra were normalized by the current from freshly evaporated gold on a fine grid positioned upstream of the main chamber. The spectra were aligned to a beamline reference material for the corresponding edge, and normalized using a linear background.

^{27}Al MAS NMR experiments were performed at 11.7 T (500 MHz) using a Bruker Avance III spectrometer operating at a Larmor frequency of 130.318 MHz. A rotor-synchronized echo pulse sequence ($\pi/2$ - τ -π - acq.), where $\tau= 1/\nu_r$ (spinning frequency), was used to acquire the spectra with a 2.5 mm probe at spinning speed of 30 kHz. A pulse width of 1.0 μs and a pulse delay of 2 seconds were used. The spectra were referenced to 1M $Al(NO_3)_3$ at 0 ppm. ^7Li MAS NMR spectra were acquired at a magnetic field of 7.02 Tesla (300 MHz) on a Bruker Avance III HD spectrometer operating at a Larmor frequency of 116.700 MHz. A rotor-synchronized echo pulse was used to acquire the spectra with a 1.3 mm probe at a spinning speed of 60 kHz. A pulse width of 1.6 μs and a pulse delay of 0.2 seconds were used. The spectra were referenced to 1M LiCl at 0 ppm and all experiments were performed at constant temperature of 283K.

2.3. Electrochemical measurement

The electrochemical properties were measured on composites containing the spinel nanocrystals as working electrodes. Electrode slurries were prepared by mixing active materials and carbon black (Denka) in 6 wt% of a solution of polyvinylidene difluoride (PVDF, Kynar) in N-methylpyrrolidone (NMP, Sigma-Aldrich), to result in 80:10:10 wt % of the three components (oxide, carbon, polymeric binder). Then, the slurry was casted on electrochemical-grade aluminum foil using a doctor blade, and dried under vacuum at 80 °C overnight to evaporate solvent moieties. The loading level in the dry electrodes was ~ 3.5 mg/cm^2. Circular pieces with a diameter of ½ inch were punched and assembled in two-electrode coin cells in a glovebox filled with Ar gas (the level of contents of water and oxygen were ≤ 0.1 ppm). Three coin cells were prepared for each sample to generate statistical significance. High purity lithium foil (Product No. 10769, Alfa Aesar) and 25 μm-thick polypropylene membrane (Celgard 2400) were the counter/reference electrode and separator, respectively. The electrolyte (BASF) consisted of 1 M $LiPF_6$ in a 3:7 (wt%/wt%) mixture of ethylene carbonate (EC) and ethyl methyl carbonate (EMC). Electrochemical measurements were performed on a Biologic BCS-805 at room temperature, or a VMP3 if cycled at 50 °C. The charge and discharge cutoff potentials were 4.3 and 3.5 V, respectively. All potentials in this report are referenced to the Li^+/Li^0 couple. The rate, *C/n*, was defined as the current density required to achieve a theoretical capacity of C = 148 mAh/g in n hours. The rate capability measurement was performed by fixing the charge current to C/10 while discharge currents were varied from C/10 to 10 C.

3. RESULTS AND DISCUSSION

Colloidal MnO nanocrystals were prepared by thermal decomposition in oleylamine, which plays a role as surface-stabilizing ligand and high boiling point solvent.[16] Al oxide layers were grown by thermal decomposition of a molecular precursor while the nanocrystals were in dispersed form to ensure even surface coverage. Bare and core-shell (CS) MnO presented powder X-ray diffraction patterns (Figure 1a) consistent with a disordered cubic rock-salt structure (JCPDS card number: 24-0735) without visible impurities. Reaction with lithium acetate at 600 °C for 4 hours in air was used to produce $Li_{1+x}Mn_{2-x}O_4$ cores. The annealing temperature was tailored to produce the phase of interest while minimizing crystal coarsening. The resulting XRD patterns matched well with the expected a cubic spinel structure (Figure 1b), with a minor impurity of Mn_2O_3 (JCPDS card number: 35-0782) in some cases. This impurity is common during the synthesis of this active oxide.[14] The Li/Mn ratio in the precursor mixture was adjusted to account for the presence of Al to maximize the content of redox-active Mn^{3+} in the $Li_{1+x}Mn_{2-x}O_4$ cores, by correlating the resulting cell parameters of the spinel structure to variations with x established in the literature (Figure S1 and Table S1).[14] At each Al content, the Li/Mn was set to get the highest cell parameter value while avoiding other impurities. The lattice parameters of the materials at the optimized Li/Mn precursor ratios varied between 8.208 and 8.222 Å depending on the Al^{3+} content in the specific sample (Table S1), corresponding to x values between 0.07 and 0.05, respectively. This result implies all samples studied electrochemically below contained similar bulk structures.

Figure 2 shows representative electron micrographs and histograms of crystal size for MnO, bare $Li_{1+x}Mn_{2-x}O_4$ and a representative set of core-shell $Li_{1+x}Mn_{2-x}O_4$ nanocrystals (CS-LMO 3). In all cases, the nanocrystal size was around 60 nm, without significant growth upon calcination. A subtle trend toward increased agglomeration of the nanocrystals was found upon calcination, which could reflect the induction of particle necking at the annealing temperature. No obvious changes in the overall morphology of the nanocrystals were observed upon introduction of Al-rich shells, either by TEM or SEM (Figure S2). The average Al content was measured by elemental microanalysis via SEM-EDX over a field of particles, which showed an increase in Al concentration with the amount of aluminum acetylacetonate solution injected, shown in Figure S4 and Table S1. The atomic ratios, defined as Al/(Al+Mn), were 0.02, 0.03 and 0.09 in CS-LMO 1, 2 and 3, respectively. These values correspond to approximately 30-50 % of Al precursors having reacted to form a coating on the colloidal manganese oxide nanocrystals. To examine the Al distribution in individual nanocrystals, STEM-EDX mapping was carried out (Figure 3a). The map of the Mn distribution matches very closely with the image, while the Al map shows most of the signal beyond the surface of the particle, indicating the presence of a shell. The distribution of the Al within the nanocrystals was further corroborated by STEM-EDX line scans of the Mn *L* and Al *K* emission lines conducted across a single particle of CS-LMO 3 (Figure 3b). The sharp upward slope in the Al signal begins ~5 nm beneath the surface of the nanocrystal, and continues at least 5 nm beyond the boundaries of the particle. The boundary of the particle being indicated by a decrease in the intensity of the Mn signal. Similar experiments were carried out on CS-LMO 2 (Figure S3). They revealed a similar distribution of elements, and, thus, a core-shell structure, despite containing less Al ions. The combination of these observations leads to the conclusion that a contiguous Al shell existed over the entire spinel nanocrystals, even after heat treatment at 600 °C.

Atomic resolution STEM images were captured along a [110] direction for both the bare and core-shell nanoparticles, in regions including the edge of the crystals (Figure 4). The micrographs show the edge of the nanoparticles, and EELS linescans taken at points from the edge to the interior. Although the Al shell was clearly visible from EDX, examination of the crystallite edges with high resolution imaging revealed relatively little difference in atomic structure between bare and core-shell nanoparticles. From this observation, it is apparent that any aluminum that diffused into the particle did not alter the overall structure of the crystal, and most likely displaced Mn within the spinel. Variations in intensity of the cationic sites in the AB_2O_4 spinel structure were noted very near the edge of the nanocrystals (Figure 4c), often giving rise to ring-like atomic arrangements. However, similar defective arrangements were observed at the surface of other $LiMn_2O_4$ samples,[17] where they have been ascribed to local clusters resembling Mn_3O_4. These features are unlikely to be a consequence of the formation of the aluminum oxide shell, since they affect only ~2 nm of the surface, and similar atomic arrangements were also observed in the bare particles (Figure 4a, c and S4), again consistent with literature observations.[17] At the very edge of the particles, annular bright-field imaging, which is sensitive to lighter elements, indicated the presence of an amorphous layer with lower atomic weight (Figures 4 and S4). This layer, though very thin, is indicative of a pure aluminum oxide shell in addition to the epitaxial shell with Al/Mn mixing. These observations are consistent with the gradients of Al content measured by EDX linescans.

Another method of examining subtle chemical changes due to heterostructure formation was possible from electron energy loss spectroscopy (EELS, Figure 4). Variations in the valence state of Mn can be measured by examining the offset, shape, and relative peak volume of the Mn L_{II} and L_{III} edges.[18] These edges correspond to dipole-allowed transitions from Mn *2p* orbitals to unoccupied *3d* orbitals, separated by the spin-orbital interaction of the Mn *2p* core hole.[19,20] In both bare and CS-LMO 3, the onset of the Mn L_{III} edge varied by ~1 eV between the surface and the bulk, which also matched the change in the white line ratio (Figure 4). These changes are ascribed to variations in valence from $Mn^{3+/4+}$ in the bulk, to $Mn^{2+/3+}$ at the surface. A plot of Mn L_{III}-edge position, measured as the difference between the oxygen K edge and the Mn L_{III}-edge through single particle indicates that the reduced surface layer was under 5 nm for this particle (Figure S5). Considering that the microscopic analysis revealed a spinel atomic arrangement wherever Mn is present, this observation would be consistent with the possible presence of Mn^{2+} defects in the tetrahedral site of the spinel framework of the shell of the nanocrystals, possibly produced during calcination, thus resembling Mn_3O_4 (or, most likely, $Mn_{3-x}Li_xO_4$) locally, as proposed in the literature.

Mn *L*- and O *K*-edge X-ray absorption spectroscopy (XAS) were measured using both a TEY detector, sensitive to ~5 nm into the powder surface, and TFY detector, which probes ~100 nm deep and, thus, is dominated by the bulk of the sample (Figure 5). TFY data were affected by self-absorption of the escaping fluorescent photons by the material, which results in different intensity ratios of the signals compared to TEY, without corresponding chemical changes. While similar to EELS, the higher energy resolution of the Mn $L_{II,III}$-edge XAS revealed two groups of multiplets with very fine structure (Figure 5a).[21] The overall shape of the spectra for the two samples was comparable when collected with the same detector. Therefore, both samples had Mn in rather similar oxidation states, consistent with the similar unit cell volumes. In contrast, the fraction of intensity of the signals in the TEY spectra positioned at absorption energies around 638.5 eV was always greater than in the TFY spectra of the same sample. Since signals at this energy are associated with the presence of Mn^{2+} ions,[22] the result confirms the slightly reduced state of Mn at the surface of both bare and modified spinels proposed from the EELS analysis.[23] The intensity (branching) ratio of I (L_{III})/I ($L_{III} + L_{II}$) is indicative of the electronic environment of Mn ions. In the case of CS-LMO 3 nanocrystals, the ratios were 0.657 and 0.542 in TEY and TFY mode, respectively, which were higher than the values of bare spinel (0.628 and 0.527) in a significant manner (Figure S6). The large branching ratio corresponds to high spin states of Mn ions with decreasing formal valences of Mn ions. The results suggest that, compared to the bare material, CS-LMO 3 is in a subtly more reduced state in the bulk and on the surface than the bare nanocrystals, likely driven by the introduction of Al.

O *K*-edge XAS represents the transition of a *1s* electron in oxygen to a *2p* level hybridized with the *3d* orbitals of Mn ions with a low spin electronic configuration. A pre-edge absorption between ~527 and 534 eV was predominant in all samples, which represents the transition of a *1s* electron in oxygen to a *2p* hybridized with the *3d* orbitals of Mn ions. Therefore, it is very sensitive to changes in formal oxidation state of the metal. The signal around 531 eV was found to be higher in the TFY spectra of bare spinel compared to TEY. Comparison with reference O *K*-edge spectra for Mn^{2+}/Mn^{3+} and Mn^{4+} in a spinel structure further suggests a more reduced state of Mn in the surface than the bulk (Figure 5b).[22,23] The degree of difference was much smaller for CS-LMO 3, which would imply that the surface reduction is slightly more pronounced without the presence of the shell. In addition, the two broad peaks above 535 eV in the O *K*-edge were assigned to the transition to hybridized states between O *2p* and Mn *4s*/*4p* or/and Li *2s* bands, as well as mostly ionic O states arising from any aluminum oxides in the shell or at the interface. These broad bands were more intense in the TEY spectrum of the core-shell materials than the bare, as expected from the formation of aluminum oxides on the surface.

Further insight into structural changes induced by the introduction of Al shells, especially local environment, was gathered with solid state magic angle spinning nuclear magnetic resonance (MAS NMR). Previous studies on spinel manganese oxides reported that lithium ions in the tetrahedral site give rise to ^{7}Li MAS NMR peaks in the 400-900 ppm range, with higher oxidation states leading to greater shifts.[24] These large shifts are ascribed to hyperfine (or Fermi-contact) interactions between the paramagnetic ion and the lithium s-orbital. As seen in Figure 6, the ^{7}Li NMR spectrum of bare $Li_{1+x}Mn_{2-x}O_4$ was dominated by a resonance at ~ 514 ppm, assigned to tetrahedral lithium environment in the ideal tetrahedral (8a) position of corresponding to domains of spinel structure where the Li/Mn ratio was ½. Three additional peaks were observed at ~ 556, 590 and 647ppm at intensity ratios consistent with the $Li_{1.05}Mn_{1.95}O_4$ composition extracted from analysis of the unit cell parameter by XRD.[24] Therefore, they were associated with the preference for the formation of local Li^+-Mn^{4+} clusters associated with the excess of Li^+ ions in the material, based on literature reports.[25] Significant changes were observed in the ^{7}Li NMR spectra of the core-shell nanocrystals. As seen in Figure 6b, the introduction of the thinnest Al shell, in CS-LMO

1, resulted in the collapse of the small resonances into a single broad shoulder, concomitant to the broadening of the main signal, which also shifted downfield, to 509 ppm. A very small peak was also detected around -1 ppm. Such diamagnetic peak could be assigned assigned to Li domains in the shell surrounded only by Al. No clear signals around ~0 ppm could be resolved for all other core-shell samples due to overlap with the broad spinning sidebands of the hyperfine signals in this spectral region (Figure 6c). CS-LMO 2 and 3 showed very similar spectra. Introduction of additional Al induced further broadening of the main ^{7}Li resonance, at 515 ppm, which was asymmetric toward high fields; no other signals could be resolved. Comparison of relative peak intensities when the data was normalized to the mass of the sample showed that the lithium resonances associated with defects driven by Li excess (observed at 556, 590 and 647 ppm for bare $Li_{1+x}Mn_{2-x}O_4$) disappeared and/or shifted to lower frequencies, merging with the main resonance. The increased broadening with the introduction of the shell is ascribed to an increase atomic disorder, for instance through lithium substitution into the vacancy and defect sites, which broke the tendency for Li^{+}-Mn^{4+} clustering in bare $Li_{1.05}Mn_{1.95}O_4$. The formation of Al-rich shells could contribute to the observed structural disorder. As Al incorporates into the shell, it intermixes with Mn within a spinel oxide framework, leading to new surface and subsurface domains where varying concentrations of diamagnetic Al^{3+} are introduced in the coordination sphere of Li at different depths into the particle. This change would reduce the magnitude of the hyperfine shift of the corresponding Li environments. No unique peaks associated with Al^{3+}-rich environments could be resolved, suggesting that it is located randomly in the structure, not through formation of clusters around Li. The smaller shift in core-shell than bare samples could also reflect subtle changes in local bond geometries around Li as a result of disorder. The changes certainly cannot be ascribed to an increased excess of Li in $Li_{1+x}Mn_{2-x}O_4$ when going from bare to core-shell, since the ^{7}Li signals have been found to shift to higher fields with x, to as much as 840 ppm, because of the increased oxidation state of Mn in the bulk.[26]

The ^{27}Al MAS NMR spectrum of CS-LMO 3 (Figure 7) showed a broad, distorted peak spanning from 100 ppm to -50 ppm, which was a combination of multiple resonances. Modelling of the data resolved at least four different ^{27}Al peaks with isotropic chemical shifts at ~ 9, 20, 44 and 89 ppm (Figure S7). Comparison of the individual line shapes, simulated quadrupole coupling constants and chemical shift values to literature studies suggested the presence of Al in 6-fold coordination sites of Al_2O_3 (8.8 ppm) and $LiAlO_2$ (19.4 ppm), as well as 5-fold coordination in Al_2O_3 (43.5 ppm) and tetrahedral Al in $LiAlO_2$ or distorted 4- coordinated aluminum oxide sites within the domain boundaries (89 ppm).[27] These species likely form the thin amorphous shell detected by high resolution STEM (Figures 4 and S4). The existence of $LiAlO_2$ would also confirm that some of the ^{7}Li intensity around 0 ppm (Figure 6) in all core-shell samples is indeed due to Li in Mn-free portions of the Al-rich shell. A large spinning sideband manifold was also observed in the ^{27}Al MAS NMR spectrum (Figure 7a). These spinning sidebands are partially due to electron dipolar (through-space) interaction containing information on the interaction of these aluminum environments with the paramagnetic Mn centers in the material. Therefore, the broad and intense manifold reflects the close physical proximity between the Al species and these Mn centers, as expected from the formation of shells on the spinel cores.[28] Similar to ^{7}Li MAS NMR, any Al in the spinel lattice would have paramagnetic Mn in the first or second coordination shell, which should give rise to signals at large shifts due to the hyperfine interaction. No such resonances were observed in the sample within the wide spectrum ranges studied. It cannot be discarded that signals exist below the detection limit of the measurement, based on the low Al content in a narrow region of co-existence of Mn and Al observed in the EDX line scans (Figure 3b), coupled with the expectation of large signal broadening due to the strength of the dipolar coupling between the Al nucleus and the unpaired electron density of Mn centers.

The electrochemical performance as cathodes of bare and core-shell nanocrystals were evaluated in half cells with Li metal. At each Al/Mn ratio, the specific capacity of the electrodes decreased with increasing Li/Mn ratio in the reaction mixture (Figure S8a-d), consistent with the increase in x in the $Li_{1+x}Mn_{2-x}O_4$ core revealed by XRD above. Figure 8a shows the potential versus electrochemical profile of the first cycle of cells containing the bare and core-shell samples with highest capacity at each Al/Mn ratio (i.e., CS-LMO 1, 2 and 3), collected at room temperature. Incremental capacity plots, dQ/dV, versus potential (Figure 8b) of the bare oxide showed two distinct peaks at around 4.02 and 4.14 V upon charging, and 3.98 V and 4.11 V upon discharging, a typical feature of $Li_{1+x}Mn_{2-x}O_4$ with low x.[29] All charge and discharge potentials were found higher, in a significant manner, in CS-LMO 2 and 3 than bare. In the case of CS-LMO 3, the difference was highest, at ~30 mV. In contrast, the difference in redox potential between CS-LMO 1 and bare, as observed in the incremental capacity plots, was very subtle. The fact that increases were observed both in charge and discharge implies the existence of an increased thermodynamic redox potential with Al content in the heterostructure. Kinetic overpotentials would shift the redox steps in charge and discharge in opposite directions, increasing the separation in potential between the two anodic and cathodic sweeps. The potential shift was also not consistent with the changes observed when x is increased in $Li_{1+x}Mn_{2-x}O_4$, which involve merging of the two redox steps (Figure S8e, f).[30] This enhancement of the thermodynamic redox potential is intriguing because it results in an increase of the energy density of the cell. The origin of this effect is unclear. Mechanisms derived from alterations of the location of the redox-active O *2p*-Mn *3d* hybrid bands due to the presence of Al in the lattice, as reported for $LiCo_{1-x}Al_xO_2$,[31] may be a contributor, although such shifts have not been observed in bulk $LiAl_xMn_{2-x}O_4$ solid solutions in the literature, even at x greater than introduced here.[32-35] Furthermore, since most Al was found to be located in the shell rather than the bulk of the nanocrystals, other effects in the bulk ensemble cannot be discarded.[36] It is tempting to speculate that this observation is related to the changes in local Li structure revealed by NMR (Figure 6), since different local environments will alter the chemical potential. The structural disordering observed with the introduction of Al shells would certainly explain the smearing of each redox plateau, and corresponding peaks of dQ/dV. The smearing could signify a change in the order of the transformation between pristine and charged states, which will be explored in follow-up work. The reversible specific capacities slightly declined with Al content. Bare LMO delivered 108 mAh/g after the first discharge, and the capacities of CS-LMO 1, 2 and 3 were 2.6, 3.5 and 6.4 % lower. Similar effects were observed in our previous study.[13] After 100 cycles at room temperature, the capacity retention of CS-LMO 1, CS-LMO 2 and CS-LMO 3 was 77.2 % (87.3 mAh/g), 78.9 % (83.1 mAh/g) and 89.5 % (91.6 mAh/g), respectively, compared to 72.8 % (81.9 mAh/g) for bare LMO (Figure 8c and S9). Therefore, the capacities of all core-shell samples surpassed the bare material at this point. The degradation in capacity was mirrored by a significant washing out of the electrochemical profiles of bare LMO (see dQ/dV plots in Figure S10). The profiles were found to be significantly more stable as the Al content increased. CS-LMO 1 also showed significantly enhanced rate capability compared to bare LMO, delivering higher capacity even at rates as high as 10C. While CS-LMO 2 was comparable to the bare material, CS-LMO 3 showed decreased capability (Figure 8d), possibly due to the high ratio of Al^{3+} ions in the surface, thus affecting electronic conductivity.

The trends were aggravated at elevated temperature (50 °C), where side reactions between electrode surface and electrolyte are accelerated. While the voltage profiles in the first cycle were largely the same as at room temperature (Figure 9), the capacity degradation accelerated. At 50 ℃, bare LMO retained only 65.5 % (69.3 mAh/g) of its initial capacity after 50 cycles at C/10, compared to 69.8 % (73.1 mAh/g), 70.4 % (75.2 mAh/g) and 80.9 % (81.5 mAh/g) retention of CS-LMO 1, 2 and 3, respectively. The effects of Al-rich oxide shells were more significant in this harsh environment than room temperature after only 50 cycles. Evidence that the improved electrochemical performance at 50 ℃ associated with enhanced interfacial stability was provided from elemental microanalysis of multiple areas of the surface of the lithium anode after cycling at C/10, using SEM-EDX (Figure S11). Roughly four times lower atomic contents of Mn were found on the Li metal assembled with CS-LMO 3 electrode compared to bare LMO (0.48±0.08 *vs* 2.1±0.6 at%). The presence of Mn on the anode is associated with the dissolution of the transition metal ions upon degradation of the cathode-electrolyte interface during cycling, for instance, through degradation mediated by Mn disproportionation in the presence of acidic impurities.[37] These dissolved ions can migrate toward the anode, and deposit on its surface.[38] It is noteworthy that low levels of Mn dissolution were found for CS-LMO 3 despite evidence of Mn^{2+} in some particle surfaces, as evidenced by STEM-EELS (Figure 4). The result suggests that the Al-rich shells were effective at passivating the active crystal surface toward interfacial degradation.

4. CONCLUSIONS

Core-shell architectures of $Li_{1+x}Mn_{2-x}O_4$ battery cathodes were engineered at significantly larger core-to-shell volume ratios than in our initial reports, following a method of sequential colloidal growth of oxide layers, using annealing at moderate temperature to create the final heterostructure and tailor the specific chemistry of the shell. This approach allowed the tuning of the specific chemical and structural characteristics of the heterostructures, and their correlation with electrode performance. The passivating layers were a combination of thin amorphous aluminum oxides (with lithium, in some cases) with a deeper crystalline component sharing the spinel structure with the core, with gradients of Al/Mn ratio from surface to bulk. The core in all samples was tailored to result in the same amount of electrochemically active Mn^{3+} to assess the effect of varied shells. Electron spectromicroscopy revealed the existence of Mn^{2+} defects at the surface of both bare and core-shell nanocrystals. The modified spinel enhanced cycling durability with respect to materials where a shell was not present. Evidence was gathered that the differences between samples was driven by the role of the protecting surface sites in contact with electrolyte. An enhancement in the redox potential was observed with Al content, which could not be explained by conventional bulk effects, but seem to correlate to a change in local structure of the spinel core as the shell ratio increased. This intriguing effect warrants further investigation. This work expands our ability to tailor multifunctional battery architectures where phases with different roles are placed efficiently with exquisite chemical control.

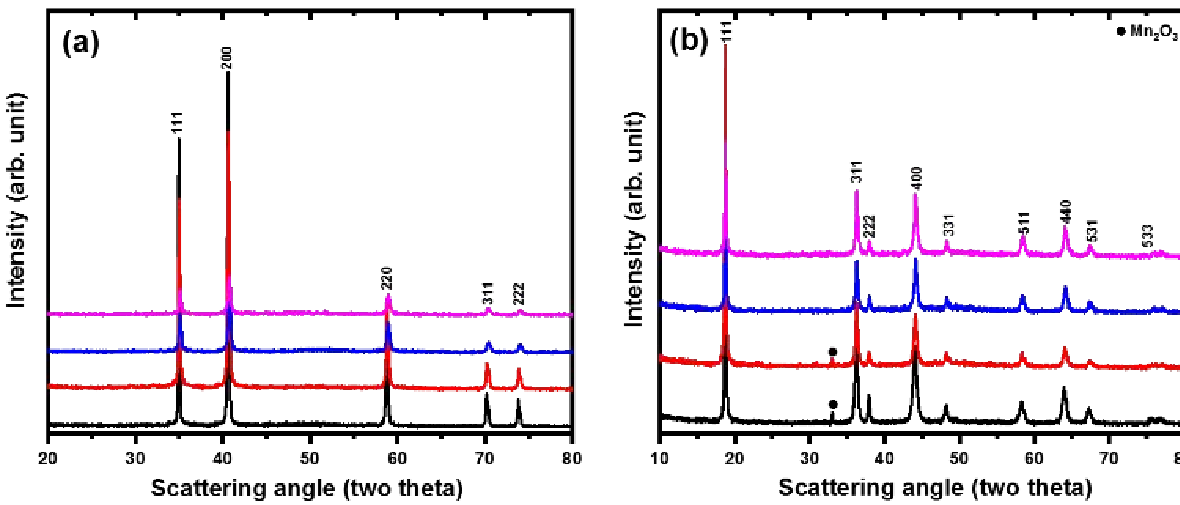

Figure 1. (a) XRD patterns of precursor disordered rock-salt oxides. (Black: bare MnO, red: CS-MnO 1, blue: CS-MnO 2, and cyan: CS-MnO 3) (b) XRD patterns of representative bare and three types of core-shell $Li_{1+x}Mn_{2-x}O_4$ spinel nanocrystals prepared by calcining at 600 ℃ with lithium acetate. (Black: bare LMO, red: CS-LMO 1, blue: CS-LMO 2, and cyan: CS-LMO 3)

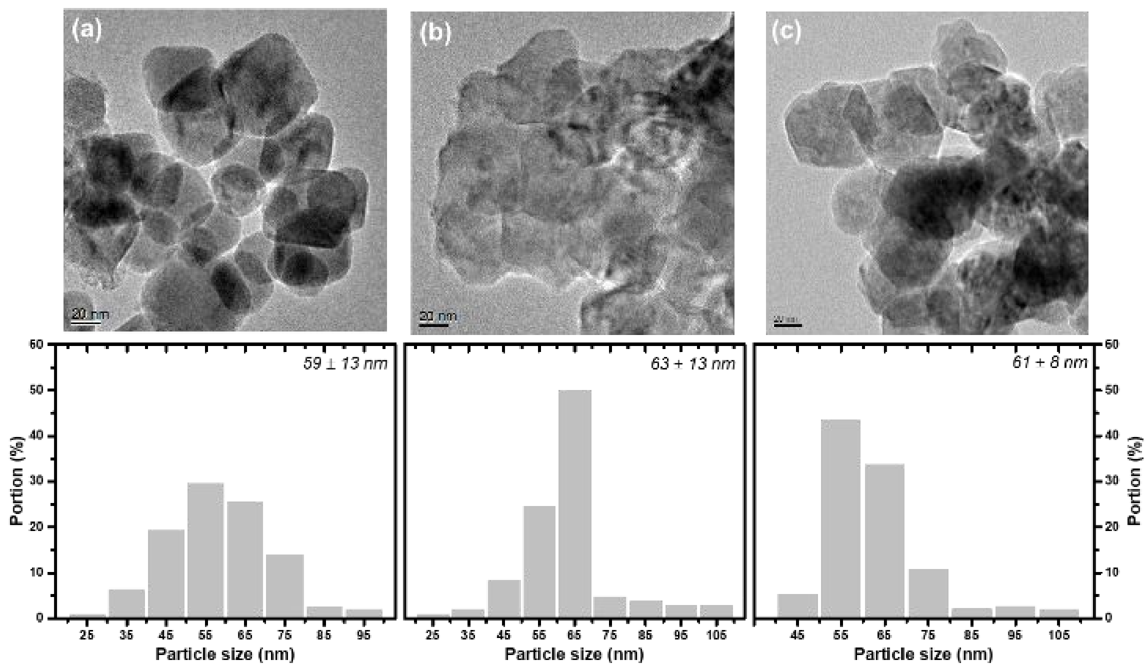

Figure 2. Representative TEM images and histograms of (a) precursor MnO, (b) bare LMO and (c) CS-LMO 3 nanocrystals. The average particle size is indicated.

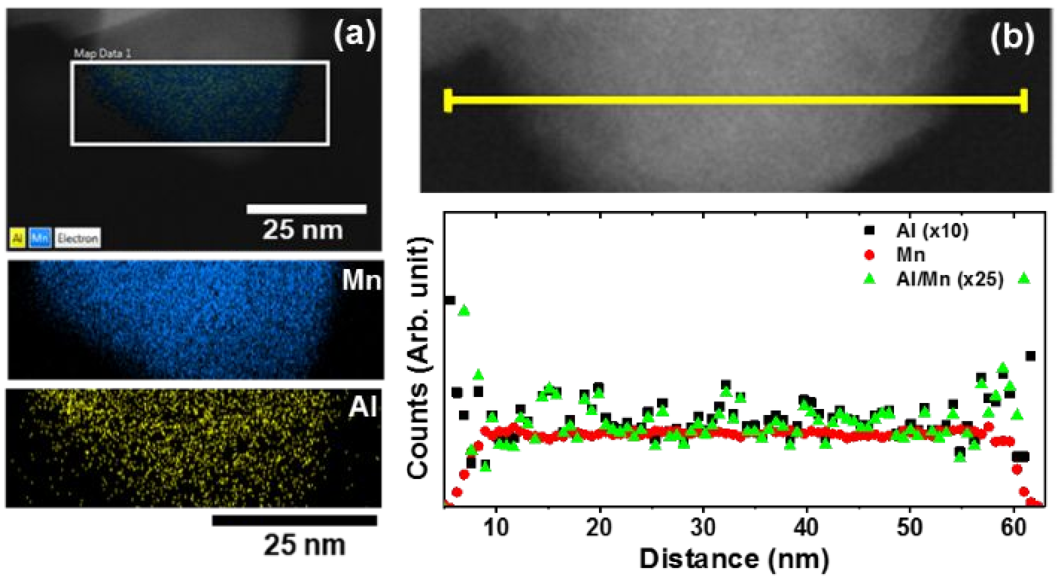

Figure 3. (a) STEM-EDX map and (b) line scan of a single CS-LMO nanocrystal.

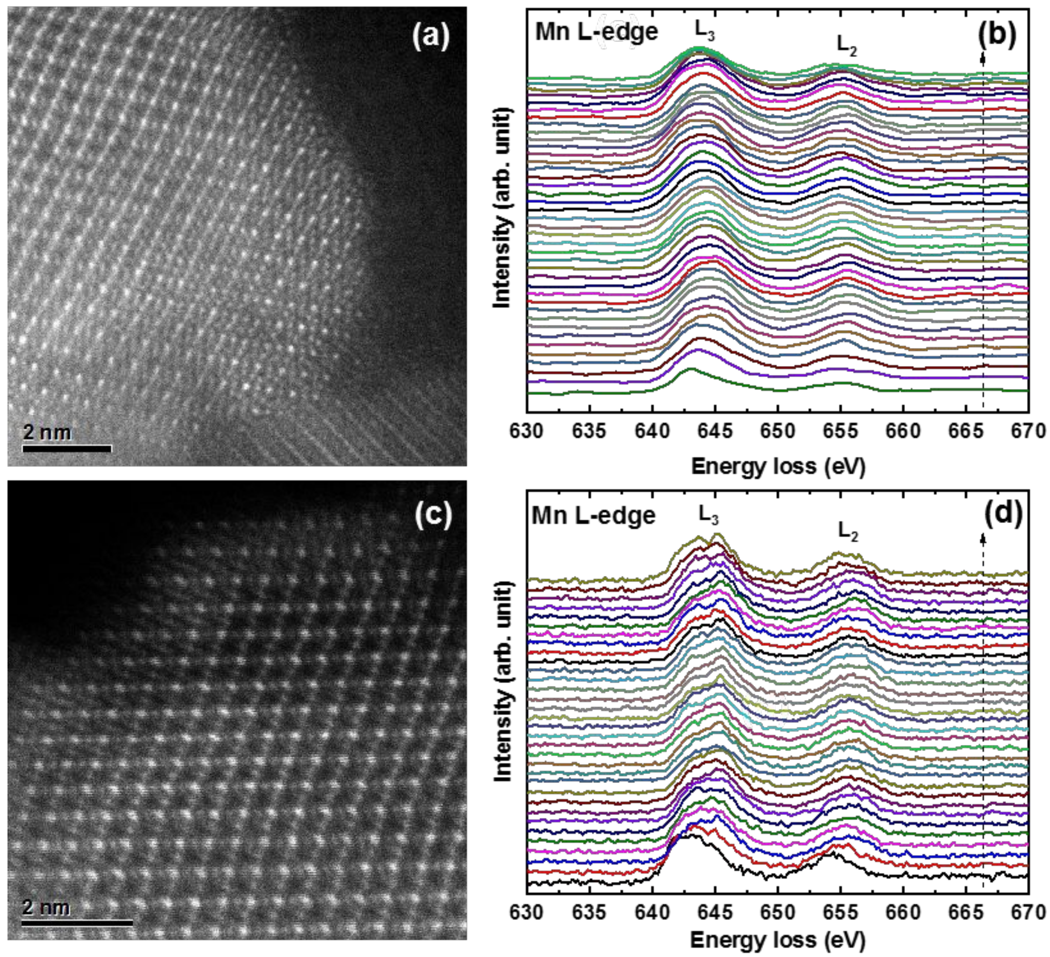

Figure 4. (a, c) LAADF image, and (b, d) Mn L-edge spectra across a single bare LMO and CS-LMO 3 nanocrystal, respectively. The arrows indicate the direction of the EELS scan, from the edge (bottom) to the interior (top) of the nanocrystal.

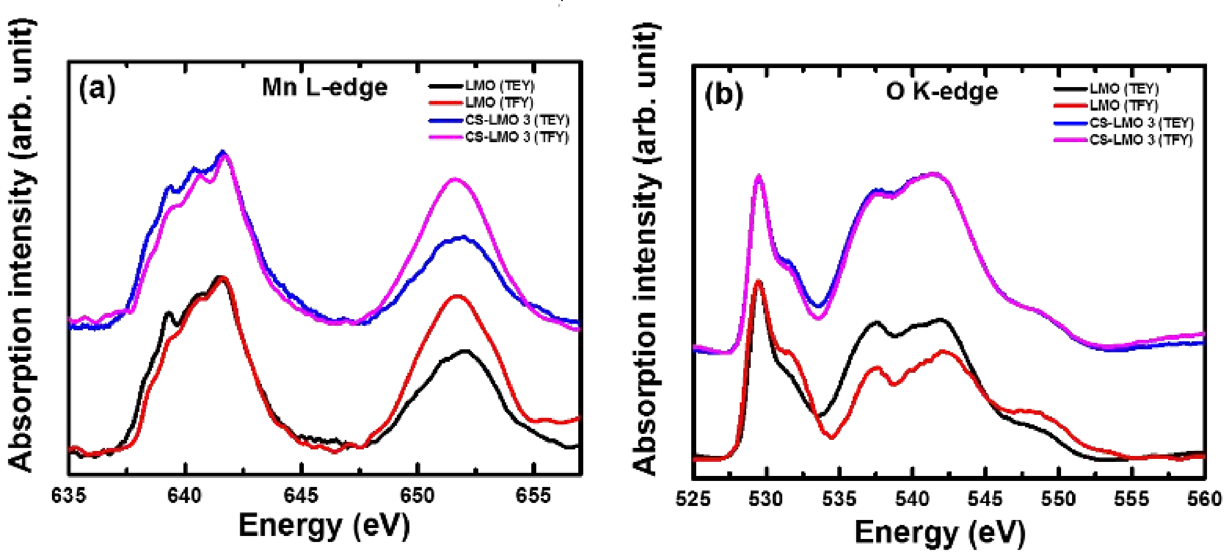

Figure 5. (a) Mn $L_{II,III}$- and (b) O K-edge of bare LMO and CS-LMO 3 nanocrystals collected in TEY and TFY mode, as indicated.

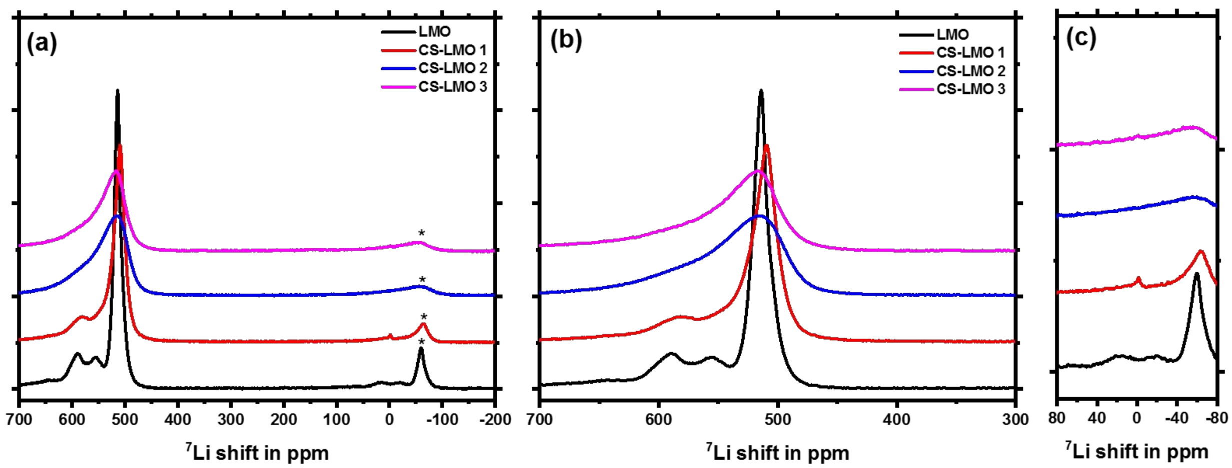

Figure 6. (a) ^{7}Li MAS NMR spectrum of bare and core-shell LMO series. (b) Magnified paramagnetic and (c) diamagnetic region in the spectra. (Asterisks indicate spinning side bands)

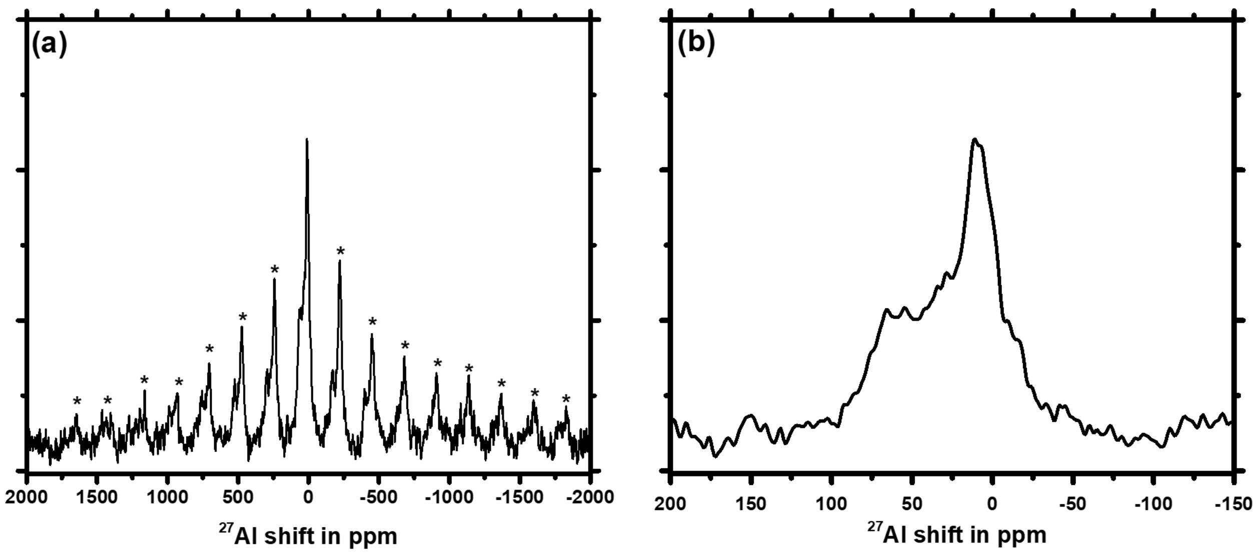

Figure 7. (a) ^{27}Al MAS NMR spectrum of CS-LMO 3 nanocrystals, and (b) magnified diamagnetic region. Asterisks indicate spinning side bands.

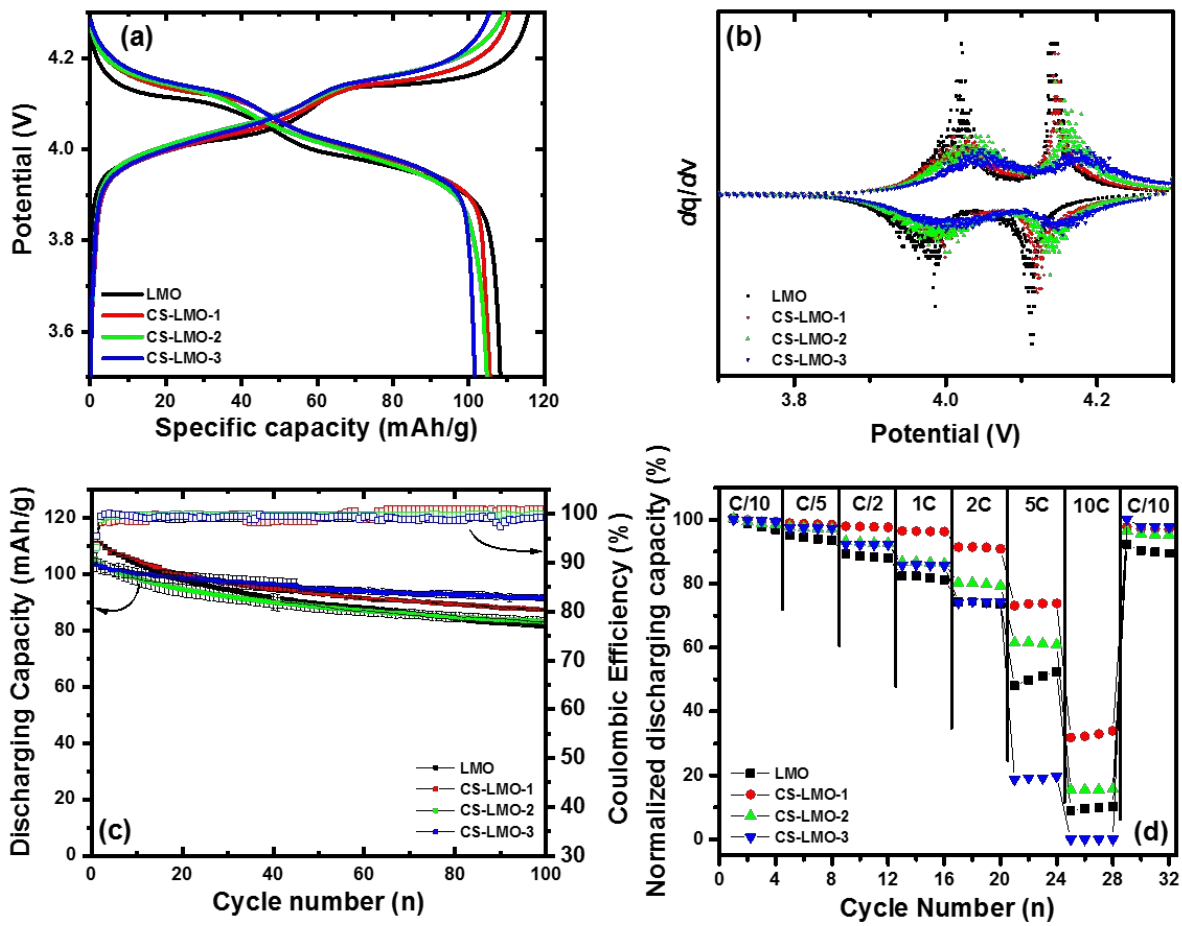

Figure 8. (a) Potential versus specific capacity profiles, (b) incremental capacity plots of Li metal half cells containing the different samples as working electrodes, cycled at C/10; (c) evolution of specific capacity (solid symbol) and coulombic efficiency (open symbol), and (d) rate capability at room temperature.

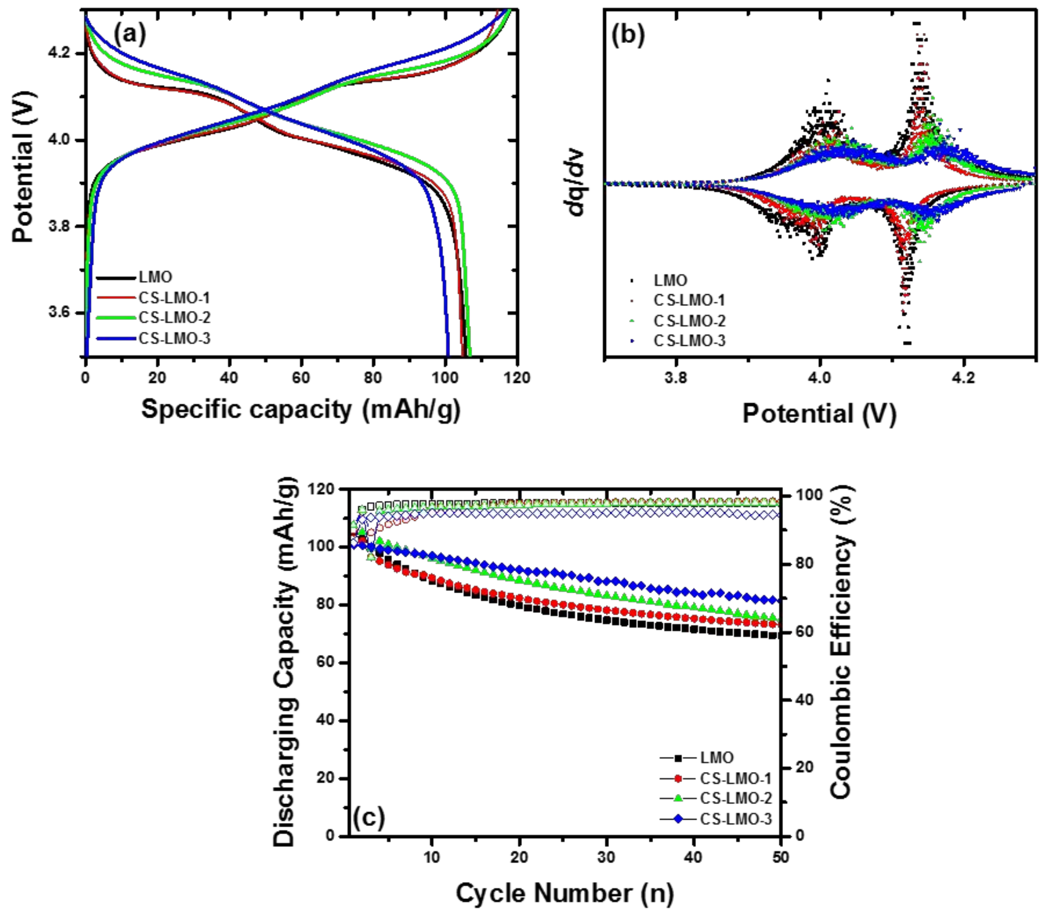

Figure 9. (a) Potential versus specific capacity profiles, (b) incremental capacity plots, (c) evolution of specific capacity (solid symbol) and coulombic efficiency (open symbol) of Li metal half cells containing the different samples as working electrodes, cycled at C/10 at 50 ℃.

AUTHOR INFORMATION

Corresponding Author

E-mail: **jcabana@uic.edu** (J.C.)

NOTES

The authors declare no competing financial interest.

Supporting Information

The Supporting Information is available free of charge on the ACS Publications website.

>> Additional XRD patterns, table of structural information, SEM images, STEM-EDX line scan, TEM image, EELS spectrums, Mn L-edge spectra, deconvoluted ^{27}Al MAS NMR spectra, electrochemical profiles, cycling retention performance, and SEM-EDX data.

ACKNOWLEDGMENTS

This work is supported by the National Science Foundation under Grant No. CBET-1605126. This work made use of instruments in the Electron Microscopy Service, JEOL JEM-ARM200CF, Research Resources Center, and University of Illinois at Chicago. The acquisition of this microscope was supported by a MRI-R2 grant from the National Science Foundation [No. DMR-0959470]. The Gatan Quantum GIF acquisition at UIC was supported by an MRI grant from the National Science Foundation (DMR-1626065). This research used resources of the Advanced Light Source, which is a DOE Office of Science User Facility under contract no. DE-AC02-05CH11231.

REFERENCES

[1] Etacheri, V.; Marom, R.; Elazari, R.; Salitra, G.; Aurbach, D. Challenges in the Development of Advanced Li-ion Batteries: a review. *Energy Environ. Sci.* **2011**, *4*, 3243-3262.

[2] Tarascon, J.-M.; Armand, M. Issue. Issues and Challenges Facing Rechargeable Lithium Batteries. *Nature* **2001**, *414*, 359−367.

[3] Hosono, E.; Kudo, T.; Honma, I.; Matsuda, H.; Zhou, H. S. Synthesis of Single Crystalline Spinel $LiMn_2O_4$ Nanowires for a Lithium Ion Battery with High Power Density. *Nano Lett*. **2009**, *9*, 1045-1051.

[4] Xu, G. J.; Liu, Z. H.; Zhang, C. J.; Cui, G. L.; Chen, L. Q. Strategies for Improving the Cyclability and Thermo-Stability of $LiMn_2O_4$-Based Batteries at Elevated Temperatures. *J. Mater. Chem. A* **2015**, *3*, 4092-4123.

[5] Aurbach, D.; Zinigrad, E.; Teller, H.; Dan, P. Factors Which Limit the Cycle Life of Rechargeable Lithium (Metal) Batteries. *J. Electrochem. Soc.* **2000**, *147*, 1274−1279.

[6] Bhattacharyya, R.; Key, B.; Chen, H.; Best, A. S.; Hollenkamp, A. F.; Grey, C. P. In Situ NMR observation of the Formation of Metallic Lithium Microstructures in Lithium Batteries. *Nat. Mater.* **2010**, *9*, 504−510.

[7] Cabana. J.; Kwon, B. J.; Hu, L. Mechanisms of Degradation and Strategies for the Stabilization of Cathode–Electrolyte Interfaces in Li-Ion Batteries. *Acc. Chem. Res.* **2018**, *51*, 299-308.

[8] Liu, H.; Wolf, M.; Karki, K.; Yu, Y.S.; Stach, E. A.; Cabana, J.; Chapman, K. W.; Chupas, P. J. Intergranular Cracking as a Major Cause of Long-Term Capacity Fading of Layered Cathodes. *Nano. Lett.* **2017**, *17*, 3452-3457.

[9] Scott, I. D.; Jung, Y. S.; Cavanagh, A. S.; An, Y. F.; Dillon, A. C.; George, S. M.; Lee, S. H. Ultrathin Coatings on Nano-$LiCoO_2$ for Li-Ion Vehicular Applications. *Nano Lett.* **2011**, *11*, 414-418.

[10] Oudenhoven, J. F. M.; van Dongen, T.; Niessen, R. A. H.; de Croon, M. H. J. M.; Notten, P. H. L. Low-Pressure Chemical Vapor Deposition of $LiCoO_2$ Thin Films: A Systematic Investigation of the Deposition Parameters. *J. Electrochem. Soc.* **2009**, *156*, D169-D174.

[11] Shim, J. H.; Lee, S.; Park, S. S. Effects of MgO Coating on the Structural and Electrochemical Characteristics of $LiCoO_2$ as Cathode Materials for Lithium Ion Battery. *Chem. Mater.* **2014**, *26*, 2537-2543.

[12] Kalluri, S.; Yoon, M.; Jo, M.; Liu, H. K.; Dou, S. X.; Cho, J.; Guo, Z. P. Feasibility of Cathode Surface Coating Technology for High Energy Lithium-ion and Beyond-Lithium-ion Batteries. *Adv. Mate*r. **2017**, *29*, 1605807.

[13] Kim, C.; Phillips, P. J.; Xu, L. P.; Dong, A. G.; Buonsanti, R.; Klie, R. F.; Cabana, J. Stabilization of Battery Electrode/Electrolyte Interfaces Employing Nanocrystals with Passivating Epitaxial Shells. *Chem. Mater.***2015**, *27*, 394-399.

[14] Paulsen, J. M.; Dahn, J. R. Phase Diagram of Li−Mn−O Spinel in Air. *Chem. Mater*. **1999**, *11*, 3065-3079.

[15] Chan, H. W.; Duh, J. G.; Sheen, S. R. $LiMn_2O_4$ Cathode Doped with Excess Lithium and Synthesized by Co-Precipitation for Li-ion Batteries. *J. Power. Sources*. **2003**, *115*, 110-118.

[16] Sun, Y. Controlled Synthesis of Colloidal Silver Nanoparticles in Organic Solutions: Empirical Rules for Nucleation Engineering. *Chem. Soc. Rev*. **2013**, *42*, 2497– 2511.

[17] Amos, C. D.; Roldan, M. A.; Varela, M.; Goodenough, J. B.; Ferreira, P. J. Revealing the Reconstructed Surface of $Li[Mn_2]O_4$. *Nano Lett.* **2016**, *16*, 2899-2906.

[18] Tan, H. Y.; Verbeeck, J.; Abakumov, A.; Van Tendeloo, G. Oxidation State and Chemical Shift Investigation in Transition Metal Oxides by EELS. *Ultramicroscopy* **2012**, 116, 24-33.

[19] Tang, D. C.; Sun, Y.; Yang, Z. Z.; Ben, L. B.; Gu, L.; Huang, X. J. Surface Structure Evolution of $LiMn_2O_4$ Cathode Material upon Charge/Discharge. *Chem. Mater.* **2014**, *26*, 3535-3543.

[20] Lin, F.; Markus, I. M.; Nordlund, D.; Weng, T. C.; Asta, M. D.; Xin, H. L. L.; Doeff, M. M. Surface Reconstruction and Chemical Evolution of Stoichiometric Layered Cathode Materials for Lithium-ion Batteries. *Nat. Commun*. **2014**, *5*, 3529.

[21] Liu, R. S.; Jang, L. Y.; Chen, J. M.; Tsai, Y. C.; Hwang, Y. D.; Liu, R. G. X-ray Absorption Studies in Spinel-Type $LiMn_2O_4$. *J. Solid. State. Chem*. **1997**, *128*, 326-329.

[22] Risch, M.; Stoerzinger, K. A.; Han, B. H.; Regier, T. Z.; Peak, D.; Sayed, S. Y.; Wei, C.; Xu, Z. C.; Shao-Horn, Y**.** Redox Processes of Manganese Oxide in Catalyzing Oxygen Evolution and Reduction: An *in Situ* Soft X-ray Absorption Spectroscopy Study. *J. Phys. Chem. C* **2017**, *121*, 17682-17692.

[23] Grush, M. M.; Horne, C. R.; Perera, R. C. C.; Ederer, D. L.; Cramer, S. P.; Cairns, E. J.; Callcott, T. A. Correlating Electronic Structure with Cycling Performance of Substituted

$LiMn_2O_4$ Electrode Materials: A Study Using the Techniques of Soft X-ray Absorption and Emission. *Chem. Mater.* **2000**, *12*, 659-664.

[24] Lee, Y. J.; Wang, F.; Grey, C. P. ^{6}Li and ^{7}Li MAS NMR Studies of Lithium Manganate Cathode Materials. *J. Am. Chem. Soc.* **1998**, *120*, 12601-12613.

[25] Lee, Y. J.; Grey, C. P. ^{6}Li Magic Angle Spinning Nuclear Magnetic Resonance Study of the Cathode Materials $Li_{1+\alpha}Mn_{2-\alpha}O_{4-\delta}$ The Effect of Local Structure on the Electrochemical Properties. *J. Electrochem. Soc.* **2002**, *149*, A103-A114.

[26] Cabana, J.; Johnson, C. S.; Yang, X. Q.; Chung, K. Y.; Yoon, W. S.; Kang, S. H.; Thackeray, M. M.; Grey, C. P. Structural Complexity of Layered-Spinel Composite Electrodes for Li-ion Batteries. *J. Mater. Res.* **2010**, *25*, 1601-1616.

[27] Han, B. H.; Paulauskas, T.; Key, B.; Peebles, C.; Park, J. S.; Klie, R. F.; Vaughey, J. T.; Dogan, F. Understanding the Role of Temperature and Cathode Composition on Interface and Bulk: Optimizing Aluminum Oxide Coatings for Li-Ion Cathodes. *ACS Appl. Mater. Interfaces* **2017**, *9*, 14769-14778.

[28] Dogan, F.; Vaughey, J. T.; Iddir, H.; Key, B. Direct Observation of Lattice Aluminum Environments in Li Ion Cathodes $LiNi_{1-y-z}Co_yAl_zO_2$ and Al-Doped $LiNi_xMn_yCo_zO_2$ via ^{27}Al MAS NMR Spectroscopy. *ACS Appl. Mater. Interfaces* **2016**, *8*, 16708-16717.

[29] Kim, D. K.; Muralidharan, P.; Lee, H. W.; Ruffo, R.; Yang, Y.; Chan, C. K.; Peng, H.; Huggins, R. A.; Cui, Y. Spinel $LiMn_2O_4$ Nanorods as Lithium Ion Battery Cathodes. *Nano Lett.* **2008**, *8*, 3948-3952.

[30] Gao, Y.; Reimers, J. N.; Dahn, J. R. Changes in the Voltage Profile of $Li/Li_{1+x}Mn_{2-x}O_4$ Cells as a Function of *x*. *Phys. Rev. B* **1996**, *54*, 3878-3883.

[31] Ceder, G.; Chiang, Y. M.; Sadoway, D. R.; Aydinol, M. K.; Jang, Y. I.; Huang, B. Identification of Cathode Materials for Lithium Batteries Guided by First-Principles Calculations. *Nature* **1998**, *392*, 694-696.

[32] Xiao, L. F.; Zhao, Y. Q.; Yang, Y. Y.; Cao, Y. L.; Ai, X. P.; Yang, H. X. Enhanced Electrochemical Stability of Al-Doped $LiMn_2O_4$ Synthesized by a Polymer-Pyrolysis Method. *Electrochim. Acta* **2008**, *54*, 545-550.

[33] Ding, Y. L.; Xie, J.; Cao, G. S.; Zhu, T. J.; Yu, H. M.; Zhao, X. B. Enhanced Elevated-Temperature Performance of AI-Doped Single-Crystalline $LiMn_2O_4$ Nanotubes as Cathodes for Lithium Ion Batteries. *J. Phys. Chem. C* **2011**, *115*, 9821-9825.

[34] Hwang, B. J.; Santhanam, R.; Liu, D. G.; Tsai, Y. W. Effect of Al-substitution on the Stability of $LiMn_2O_4$ Spinel, Synthesized by Citric Acid Sol-Gel Method. *J. Power Sources* **2001**, *102*, 326-331.

[35] Lee, Y. S.; Kumada, N.; Yoshio, M. Synthesis and Characterization of Lithium Aluminum-Doped Spinel ($LiAl_xMn_{2-x}O_4$) for Lithium Secondary Battery. *J. Power Sources* **2001**, *96*, 376-384.

[36] Zhan, D.; Liang, Y.; Cui, P.; Xiao, Z. Al-doped $LiMn_2O_4$ Single Crystalline Nanorods with Enhanced Elevated-Temperature Electrochemical Performance *via* a Template-Engaged Method as a Cathode Material for Lithium Ion Batteries. *RSC Adv.* **2015**, *5*, 6372-6377.

[37] Jang, D. H.; Shin, Y. J.; Oh, S. M. Dissolution of Spinel Oxides and Capacity Losses in 4 V Li / $Li_xMn_2O_4$ Cells. *J. Electrochem. Soc.* **1996**, *143*, 2204-2211.

[38] Lee, K. T.; Jeong, S.; Cho, J. Roles of Surface Chemistry on Safety and Electrochemistry in Lithium Ion Batteries. *Acc. Chem. Res.* **2013**, *46*, 1161-1170.

Table of Contents (TOC)